batteries

MDPI

Article

Molybdenum Vanadium Oxides as Intercalation Hosts for Chloroaluminate Anions

Kevin Bhimani [1], Aniruddha Singh Lakhnot [1], Shyam Sharma [1], Mukul Sharma [2], Reena A. Panchal [1], Varad Mahajani [3] and Nikhil Koratkar [1,3,*]

[1] Department of Mechanical, Aerospace and Nuclear Engineering, Rensselaer Polytechnic Institute, Troy, NY 12180, USA
[2] Department of Chemical and Biological Engineering, Rensselaer Polytechnic Institute, Troy, NY 12180, USA
[3] Department of Material Science and Engineering, Rensselaer Polytechnic Institute, Troy, NY 12180, USA
* Correspondence: koratn@rpi.edu

Abstract: Driven by the cost and scarcity of Lithium resources, it is imperative to explore alternative battery chemistries such as those based on Aluminum (Al). One of the key challenges associated with the development of Al-ion batteries is the limited choice of cathode materials. In this work, we explore an open-tunnel framework-based oxide (Mo_3VO_x) as a cathode in an Al-ion battery. The orthorhombic phase of molybdenum vanadium oxide (o-MVO) has been tested previously in Al-ion batteries but has shown poor coulombic efficiency and rapid capacity fade. Our results for o-MVO are consistent with the literature. However, when we explored the trigonal polymorph of MVO (t-MVO), we observe stable cycling performance with much improved coulombic efficiency. At a charge–discharge rate of ~0.4C, a specific capacity of ~190 mAh g^{-1} was obtained, and at a higher rate of 1C, a specific capacity of ~116 mAh g^{-1} was achieved. We show that differences in synthesis conditions of t-MVO and o-MVO result in significantly higher residual moisture in o-MVO, which can explain its poor reversibility and coulombic efficiency due to undesirable water interactions with the ionic liquid electrolyte. We also highlight the working mechanism of MVO || $AlCl_3$–[BMIm]Cl || Al to be different than reported previously.

Keywords: aluminum-ion batteries; high-capacity cathode; open-tunnel oxides; energy storage; ionic liquid electrolyte

Citation: Bhimani, K.; Lakhnot, A.S.; Sharma, S.; Sharma, M.; Panchal, R.A.; Mahajani, V.; Koratkar, N. Molybdenum Vanadium Oxides as Intercalation Hosts for Chloroaluminate Anions. Batteries **2023**, 9, 92. https://doi.org/10.3390/batteries9020092

Academic Editors: Amartya Mukhopadhyay and Carlos Ziebert

Received: 21 November 2022
Revised: 13 January 2023
Accepted: 25 January 2023
Published: 29 January 2023

1. Introduction

Lithium (Li) metal is considered to be the holy grail of the battery storage system, owing to its light weight and highest gravimetric energy density compared to any other battery storage system [1,2]. However, one of the most critical issues with using Li metal is its reactivity with liquid electrolytes and the non-uniform deposition of Li metal during plating, leading to poor coulombic efficiency and uncontrolled growth of dendrites, which can lead to possible short-circuiting and potential fire hazards [3,4]. Another key issue with Li-metal batteries is the scarcity of Li in the earth's crust [5]; only 0.0065% of the earth's crust is filled with Li metal [6]. Compared to Li, alternatives such as Na, K, Ca, Mg, and Al are earth abundant. Of these, monovalent Na (1165 mAh g^{-1}) and K (685 mAh g^{-1}), delivering one electron during battery operation, display relatively low gravimetric capacity compared to Li (3860 mAh g^{-1}), while multivalent systems based on Mg (2150 mAh g^{-1}), Ca (1337 mAh g^{-1}), and Al (2980 mAh g^{-1}) can deliver more than one electron during battery cycling and attain higher specific capacity [6–11]. Hence, to cater to the rising demand in portable electronics, electric vehicles, and grid storage, it is imperative that we look at these alternate multivalent battery systems [12–15].

Although Calcium has the lowest reduction potential among multivalent systems (2.87 V vs. Standard Hydrogen Electrode (SHE)), it is difficult to achieve reversible

plating and stripping of Ca metal in organic electrolytes due to the formation of an ion-insulating layer at the metal-electrolyte interface [16]. While reversible plating and stripping have been demonstrated for Magnesium metal in organic electrolytes, and although it has a low reduction potential (2.36 V vs. SHE), Magnesium metal suffers from the critical issue of dendrites that pose potential safety hazards and provides only a limited choice of electrolytes [17,18]. Aluminum, with the possibility of three electron transfers, is a promising alternative to Li-based battery systems. It is the most abundant metal in the earth's crust and significantly cheaper than Li [19]. Al metal is also not prone to forming dendrites and is chemically inert towards the liquid electrolyte, unlike Li metal. However, unlike Na and K, Al does not show reversible plating/stripping with Li-similar organic electrolytes, which has hindered the development of reversible Al-ion batteries. Reversible plating and stripping of Al were demonstrated for the first time with the use of an ionic liquid (IL) melt of Aluminum chloride ($AlCl_3$) and 1-ethyl-3-methylimidazolium chloride [EMIm]Cl [20]. Since then, most studies on non-aqueous Al batteries have been carried out using similar IL electrolytes [21–23]. A number of advantages exist for these ILs, including high ionic conductivity, thermal and chemical stability, and a wide electrochemical stability window [24]. IL electrolytes are also non-flammable and non-volatile, which makes them better candidates for rechargeable Al-ion batteries.

The working mechanism of these batteries differs from the rocking chair mechanism of conventional Li-ion batteries [6,21]. Instead of Al^{3+}, $AlCl_4^-$ and $Al_2Cl_7^-$ are the active ions in this case. Some studies suggest that during charge, $AlCl_4^-$ intercalates into the host cathode, while at the anode $Al_2Cl_7^-$ is transformed into Al metal and $AlCl_4^-$. On discharge, a reverse reaction takes place, with $AlCl_4^-$ de-intercalating from the host cathode while metallic Al and $AlCl_4^-$ transform into $Al_2Cl_7^-$. Owing to the bulkiness of these anions, the space occupied in the host material is significantly greater than that occupied by small Li^+ ions, resulting in limited attainable capacity. For example, the Al/graphite cell attains a specific capacity of ~70 mAh g^{-1}, while graphite can attain over five times higher specific capacity when used with Li (~372 mAh g^{-1}) [3,21]. Some other studies suggest that during discharge the $Al_2Cl_7^-$ dissociates into Al^{3+} and $AlCl_4^-$, and it is Al^{3+} that takes part in the intercalation process [25]. However, the high charge density of Al^{3+} often results in poor reversibility during battery operation and poor rate performance due to the strong coulombic effect induced by the three positive charges of the Al cation. Hence, a key challenge in developing Al-ion batteries has been in identifying suitable cathode materials that can intercalate bulky ions with high charge density. Furthermore, significant volume changes during the charging-discharging process, due to the bulky active ions, can also lead to material pulverization and electrode delamination. Layered materials, having larger interlayer spacing, such as graphitic foam, graphene, and hexagonal-MoO_3, V_2O_5, and VO_2 have been investigated as host materials in Al-ion batteries [21,26–30]. Prussian blue analogs, due to their large pore size, have also been examined [31]. Additionally, the Chevrel phase (Mo_6S_8) has been used as a host for Al-ion batteries [32,33]. However, all the above-examined host materials either suffer from low cell voltages, low capacities, poor rate performance, or poor cyclic stability.

To overcome the aforementioned challenges, the use of open-tunnel structures based on multi-transitional redox centers, such as Mo and V, have recently been demonstrated for different multivalent battery systems such as Zn, Mg, and Ca [34–36]. Mo and V have the ability to change their oxidation state by two or more and can therefore aid in facilitating charge redistribution and maintaining charge neutrality within the host structure during the charging/discharging process. The orthorhombic phase of MVO (o-MVO) has previously been investigated as a cathode in Al-ion batteries and displays high specific capacity at elevated temperatures of ~55 C but displays poor cyclic stability and poor high rate capability at room temperature [22]. In this study, we have investigated the performance of the trigonal phase of MVO (t-MVO) as the cathode for rechargeable Al batteries, with $AlCl_3$–[BMIm]Cl as the IL electrolyte, comparing its performance to the previously reported o-MVO. Both o-MVO and t-MVO oxide materials have a layered

structure along the c-axis, while the arrangement of atoms in the a-a or a-b planes differs for the crystalline samples. These layers are stacked together by corner sharing an M-O-M (M = Mo or V) bond, giving rise to a framework structure with three-, six-, and seven-membered channels. Our results, for the o-MVO phase, conform to an earlier study and exhibit poor stability and low coulombic efficiency. By contrast, we find that the tri-phase displays much stabler performance, higher coulombic efficiency, and better rate capability than the ortho polymorph [22]. Our results suggest that the difference in performance between the two polymorphs stems from different synthesis conditions, which leads to a lower amount of residual moisture in the tri-phase of MVO, leading to better stability than the ortho phase [37]. Lastly, we demonstrate that the first cycle for the t-MVO || $AlCl_3$–[BMIm]Cl || Al should be a charge cycle rather than a discharge cycle.

2. Experimental Methods

2.1. Material Synthesis

Preparation of trigonal Molybdenum Vanadium Oxide: HPLC-grade water was used throughout the synthesis of MVO unless otherwise specified. t-MVO was synthesized via the traditional hydrothermal synthesis method. First, 50 mM of Ammonium heptamolybdate $(NH_4)_6Mo_7O_24H_2O$ (Sigma Aldrich, St. Louis, MI, USA, > 99%) was dissolved in 40 mL water and stirred vigorously in a sealed round-bottom flask, which was degassed and then purged with N_2 for 10 min. Next, 12.5 mM Vanadyl sulfate $VOSO_4nH_2O$ (Sigma Aldrich, USA, 97%) dissolved separately in 40 mL water was then added dropwise using a syringe. The solution was left stirring for another 20 min under N_2 bubbling atmosphere (to avoid excess O_2), post which a dark purple solution was obtained. The pH of the resulting solution was adjusted to ~2.2 using 2 M H_2SO_4. The solution was stirred for another 10 min and then quickly transferred to a Teflon-lined stainless steel autoclave for the hydrothermal reaction. The reaction was carried out at ~175 C for 20 h in an oven and reactor was left to cool down overnight. The solution was vacuum filtered and was allowed to dry overnight at ~80 C in a vacuum oven. The filtered product was treated with 0.4 M oxalic acid at ~60 C for half an hour to remove any amorphous impurities. The oxalic acid treated powder was vacuum filtered and dried overnight in a vacuum at ~80 C and, subsequently, the powder was calcined at ~400 C for 2 h to remove residual H_2O and NH^+ molecules. The furnace was then allowed to cool down naturally. Synthesis of ortho phase followed a similar procedure except pH adjustment was not required and the reaction time was 48 h.

Preparation of the IL electrolyte: Anhydrous aluminum chloride $AlCl_3$, (Alfa Aesar, Haverhill, MA, USA 99.999%) and 1-butyl-3-methylimidazolium chloride [BMIm]Cl, (Alfa Aesar, Haverhill, MA, USA 95%) salts were used as sources of the ILs. Both $AlCl_3$ and [BMIm]Cl, being highly hygroscopic, were handled inside the glovebox. [BMIm]Cl was baked at ~130 C for 12 h on a hot plate inside the argon-filled glovebox to remove the residual moisture. The reaction between $AlCl_3$ and [BMIm]Cl is highly exothermic and, consequently, to avoid a sudden rise in the temperature, the ILs were prepared by slowly adding anhydrous $AlCl_3$ to the [BMIm]Cl under continuous stirring. The mole ratio of $AlCl_3$ to [BMIm]Cl for this study was kept at 1.1. The resulting light-yellow transparent solution was left to stir overnight.

2.2. Electrochemical Measurements

The electrodes were prepared by grounding the calcined oxide powder with Super P in ratio of 5:1, then poly(vinylidene fluoride) (PVDF) pre-mixed in N-methyl-2-pyrrolidone was added such that the net composition of the slurries become 75:15:10 for the active material: Super P: PVDF. The slurry was mixed using a shear mixer at ~2000 rpm for ~20 min. The slurry was then coated on a Ti foil using a doctor blade, dried in ambient conditions for 2–3 h, and then dried at 120 C under vacuum for 12 h. Electrochemical tests were performed with a two-electrode setup on CR2032-type coin cell inside an Ar-filled glovebox (MBraun Labstar) with < 1 ppm H_2O and O_2. Whatman Glass Fiber (GF/D) filter

paper was used as separator, metallic Aluminum (Alfa Aesar, Haverhill, MA, USA 99.999%, 0.25 mm thickness) was used as a counter and reference electrode, and $AlCl_3$–[BMIm]Cl IL as the electrolyte. Ti foils were used as liner material inside the stainless steel casing to prevent corrosion from the acidic electrolyte. Galvanostatic charge-discharge tests were performed using Arbin BT2000 battery instrument within a voltage window of 0.02 V to 2.4 V. Cyclic voltammetry was conducted at room temperature within the same voltage range using Gamry Reference 3000 potentiostat (PA, USA).

2.3. Material Characterization

To determine the crystal structure of the different polymorphs of MVO particles, X-Ray diffraction (Panalytical X'pert PRO MPD system (USA) with Cu K radiation (= 1.54 Å)) was performed in a 2-theta range of 5 to 60 and a step size of 0.04. The morphology of the powder as well as the electrode samples were analyzed by scanning electron microscopy (SEM), and elemental distribution spectroscopy (EDS) mapping was conducted on a Carl Zeiss Supra 55 field emission SEM. X-Ray photoelectron spectroscopy (XPS) was conducted on a PHI 5000 Versa probe system (MN, USA) equipped with Al K radiation (~1486 eV). For the ex-situ analysis, all the cycled cells were disassembled inside the Ar-filled glove box and the electrodes were washed with Methanol and dried for 2 h on a hot plate at ~80 C before further characterization. Thermogravimetric analysis (TGA) was performed on a TA Instruments Q50 thermogravimetric analyzer with a heating rate of ~2 C min^{-1} in air atmosphere. The Raman spectra were taken using 3 mW of 532 nm laser as excitation source and 100 s of integration time using Andor Shamrock SR-500i (EU) imaging spectrometer.

3. Results and Discussion

MVO powders were synthesized via traditional hydrothermal synthesis using polyoxometalate (POM)-based chemistry, as described in the literature [37,38]. A schematic of the overall process is shown in Figure 1a and described in detail in the Experimental Methods section. Here, Mo_6O_{21} is the building block, and different reaction conditions such as pH, time, temperature, and pressure lead to the formation of different final structures. t-MVO is obtained by tuning the pH of the mixed solution of Ammonium heptamolybdate and Vanadyl sulfate to ~2.2 with a reaction time of 20 h. To obtain the ortho phase, a reaction time of 48 h is required without tuning the pH of the solution. The insets in Figure 1b,c show
the crystal structure of t-MVO and o-MVO. Both polymorphs exhibit large "hexagonal" and "heptagonal" pores (5–6 Å), which can possibly accommodate bulky $AlCl_4^-$ anions.

X-ray diffractograms shown in Figure 1b,c confirms the formation of the desired phase. Two diffraction peaks at ~22.2 and 45.3 were observed for both samples. These are characteristics of (001) and (002) planes indicating a layered structure (along the c-axis) with the same lattice distance of about ~0.4 nm. The peaks at a low angle (<10) differentiate both materials and highlight the different arrangement of atoms in the a-b plane (inset pictures of Figure 1b,c). The trigonal MVO shows two characteristic peaks at 8.3 and 9.5 corresponding to the (110) and (200) planes, while the orthorhombic MVO displays three characteristic diffraction peaks at 6.6, 7.9, and 9.0, corresponding to (020), (120), and (210) planes as reported earlier in the literature [39,40]. The a-b planes in both materials are connected by M O M (M = Mo or V) bonds along the c-axis.

The scanning electron micrographs of the as-prepared electrodes are shown in Figure 1d,e. Both the tri- and ortho polymorphs of MVO are long rods with lengths ranging from ~4 to 10 m and diameters ranging from ~400 to 700 nm. To understand the distribution of Mo, V, and O, elemental EDS maps were constructed as shown in the insets of Figure 1d,e. The results clearly demonstrate the uniform distribution of Mo, V, and O in both compounds. The valence of Mo and V was analyzed by XPS. The XPS survey spectra of both the polymorphs (Figure S1a,b) show almost an identical spectrum. As will be discussed later, the high-resolution Mo 3d spectra of both the o-MVO and t-MVO phases in pristine electrodes indicate Mo to be present in +6 and +5 oxidation states, whereas the high-resolution V 2p spectra indicate V to be in +5 and +4 oxidation states. Raman spectroscopy of both materials was also conducted to

analyze their vibrational modes. The obtained spectra are shown in Figure S2. In both t-MVO and o-MVO, a main band at ~870 cm ^{1} was observed, indicating the presence of pentagonal $\{Mo_6O_{21}\}$ units. Two weak bands at 820 cm ^{1} and 980 cm ^{1} were also observed, which can be assigned to Mo O Mo vibrations and Mo=O and/or V=O vibrations, respectively [41–43].

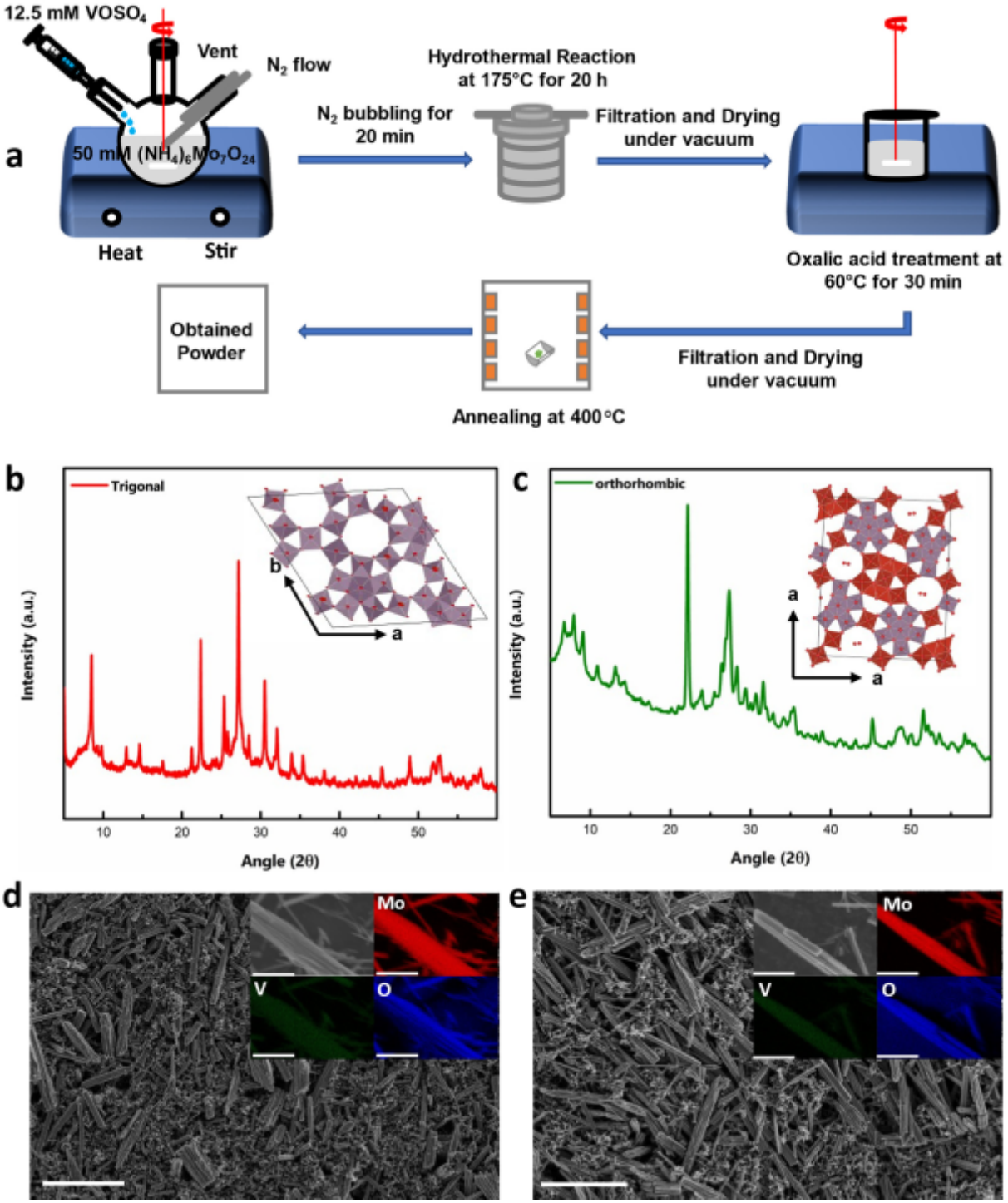

Figure 1. Synthesis and characterization of t-MVO and o-MVO samples: (**a**) Schematic of the overall synthesis process; X-Ray diffraction pattern of annealed trigonal (**b**) and orthorhombic (**c**) powder samples (inset (**b**,**c**) shows crystallographic structure of respective phases); scanning electron micrographs of assembled trigonal (**d**) and orthorhombic (**e**) electrodes (inset shows EDS maps of the distribution of Mo, V, and O throughout the rods). Scale bar is 5 m.

Electrochemical tests were performed on a CR 2032 stainless steel coin cell setup with Ti foil as a liner to prevent corrosion of the stainless steel casing from the acidic IL electrolyte. Al foil was used as a counter and reference electrode. A schematic drawing of the working Al/MVO cell during the discharge cycle is shown in Figure 2a. On the cathode side, $AlCl_4^-$ de-intercalates from the MVO host, while at the anode $AlCl_4^-$ and metallic Al are transformed into $Al_2Cl_7^-$. Figure 2b represents the cyclic voltammogram (CV) of the t-MVO, carried out at a scan rate of 0.1 mV s^{-1}. During the first anodic scan, the CV profile shows a broad peak at ~1.34 V, while in the subsequent cycles, the anodic peak appears at a lower voltage of ~0.9 V. We hypothesize that this initial high activation potential corresponds to resistance to insertion of the bulky $AlCl_4^-$ anions into the host MVO structure. Once the pores are activated, the resistance to the insertion decreases, and, correspondingly, the insertion potential decreases to ~0.9 V. The broad peak corresponds to the reduction of Mo and V, as discussed later. On the cathodic side, the peak appears at ~0.45 V. The CV profiles overlapped well after the first few cycles suggesting good reversibility. For the ortho phase, we observed a similar behavior, however, the CV profiles do not overlap suggesting poor reversibility (Figure 2c). At a higher scan rate of 0.5 mV s^{-1} (Figure S3), the separation between the anodic and cathodic peaks increases but the CV profiles still overlap for t-MVO, suggesting reversible behavior even at a higher rate. The galvanostatic charge-discharge curves at 0.4C (1C = 170 mA g^{-1}) for t-MVO and o-MVO are shown in Figure 2d,e, respectively. The results correspond well with the results observed from the CV profiles. The initial insertion plateau at a high voltage (~1.2 V) for both phases corresponds to the activation of the electrode and, subsequently, this insertion plateau appears at a lower voltage of ~0.8 V. The voltage profile for t-MVO shows good reversibility with overlapping plateaus during subsequent charge-discharge cycles, while the o-MVO phase displays poor reversibility as indicated by non-overlapping charge-discharge curves. We would also like to highlight from our results that in the case of MVO || IL || Al, the first cycle is a charge wherein the $AlCl_4^-$ ion inserts into the pores of the MVO, and on discharge the $AlCl_4^-$ de-inserts from the cathode. This is supported by the near negligible discharge capacity (~25 mAh g^{-1}) if the first cycle is a discharge cycle (Figure S4), while the first discharge capacity is seven times higher (~180 mAh g^{-1}) when the first cycle is a charge cycle.

The cyclic stability of both materials at a rate of ~0.4C is shown in Figure 3a. In both cases, there is a slight increase in the initial capacity, which can be attributed to the electrode activation. Although the ortho phase displays a higher initial capacity, it shows a rapid capacity fade with cycling, while the tri-phase shows a relatively stable performance. Such rapid capacity fade for the o-MVO phase is also reported by Kaveevivitchai et al. (Figure S5) [22]. Table S1 compares t-MVO with other related cathode materials for Al-ion batteries. While the majority of reported materials show either high specific capacity or low fade rate, t-MVO stands out in its ability to deliver both high specific capacity and low fade rate [22,29,32,44–56]. Figure 3b shows the coulombic efficiency (CE) results for the data shown in Figure 3a. For the tri-phase, the CE remains stable in the range of 93–95%, while the CE for the ortho phases fluctuates between 85 and 92% and then rapidly decreases to below 70%. Lower CE implies a lack of reversibility, which correlates with the rapid capacity decline for the ortho phase. Even at a higher charge-discharge rate of 1C, a similar trend in the CE is observed with the tri-phase, displaying a stable CE of > 97%, whereas the CE of the ortho phase is much lower and fluctuates between 90 and 95% as shown in Figure S6. This CE behavior clearly demonstrates greater irreversibility for the ortho phase than the tri-phase.

We further investigated the rate capability of both phases. At a low rate of 0.2C, the tri-phase displays a high specific capacity of ~225 mAh g^{-1} as indicated in Figure 3c. At higher rates of 0.4C, 0.6C, 0.8C and 1C the tri phase exhibits a stable capacity of ~190 mAh g^{-1}, ~150 mAh g^{-1}, ~130 mAh g^{-1}, and ~116 mAh g^{-1}, respectively. A capacity of ~216 mAh g^{-1} is achieved when the rate is reduced to 0.2 C again. On the contrary, the ortho phase (Figure 3d) displays a high specific capacity of ~246 mAh g^{-1} at 0.2 C but

decreases rapidly as the rate is increased. It exhibits a capacity of ~180 mAh g ^{1}, ~116 mAh g ^{1}, ~76 mAh g ^{1}, and ~59 mAh g ^{1} at the rates of 0.4C, 0.6C, 0.8C and 1C, respectively. As the rate is decreased to 0.2C, the ortho phase is only able to attain a specific capacity of ~130 mAh g ^{1}, which further demonstrates the irreversible nature of the ortho phase.

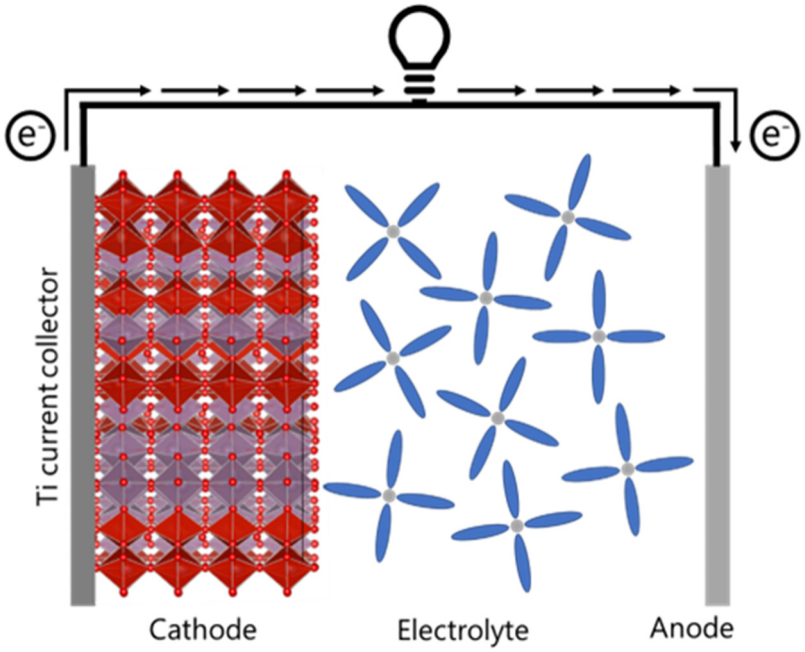

(a)

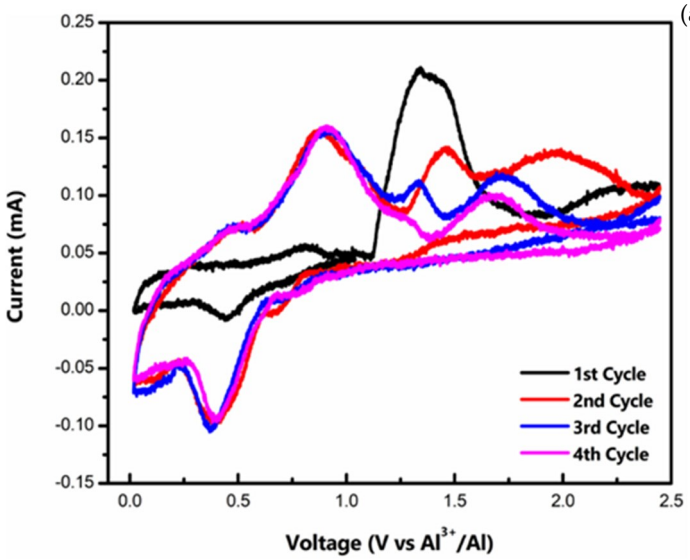

(b)

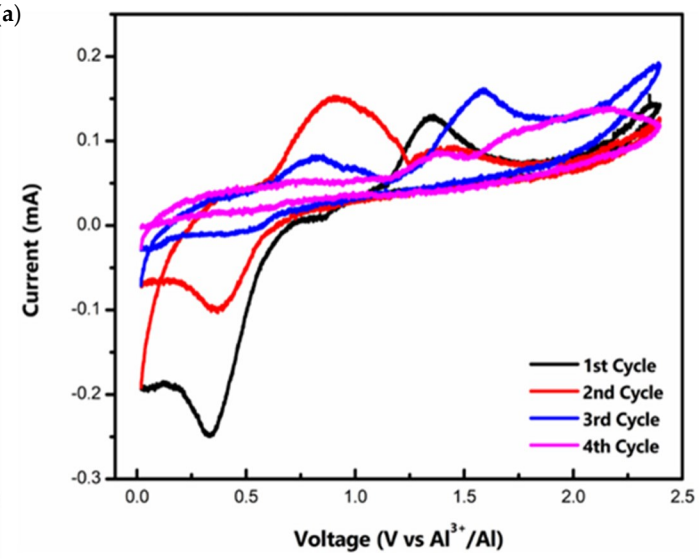

(c)

Figure 2. Cont.

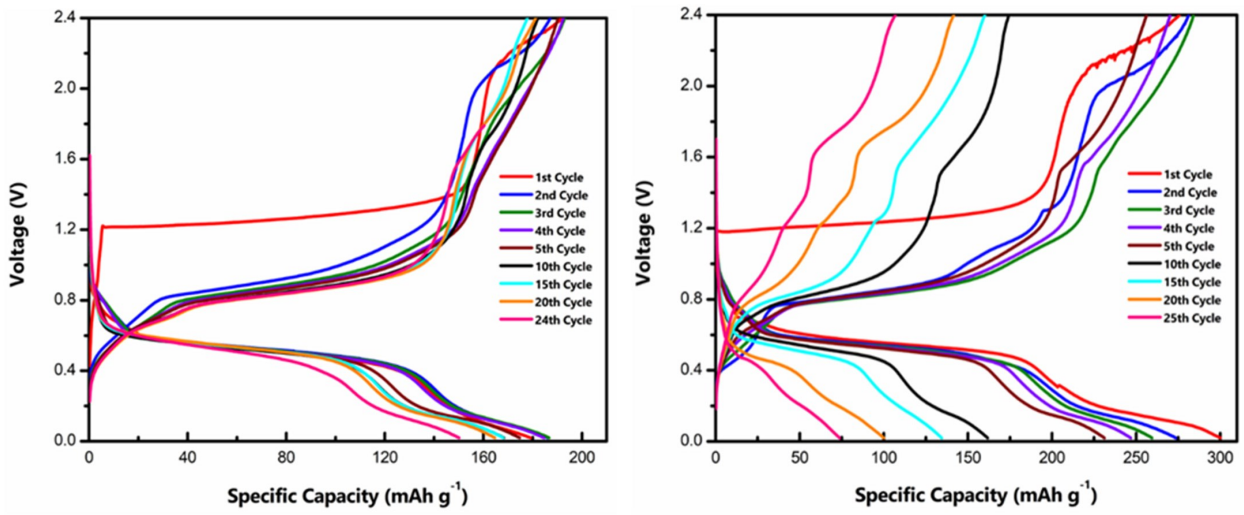

(**d**) (**e**)

Figure 2. Electrochemical characterization of MVO cathode: (**a**) Schematic drawing of Al/MVO cell during discharge; cyclic voltammogram of t-MVO (**b**) and o-MVO (**c**) at a scan rate of 0.1 mV s ^{1} in 0.02–2.45 V range; galvanostatic charge-discharge curves for t-MVO (**d**) and o-MVO (**e**) at a rate of 0.4C (1C = 170 mA g ^{1}).

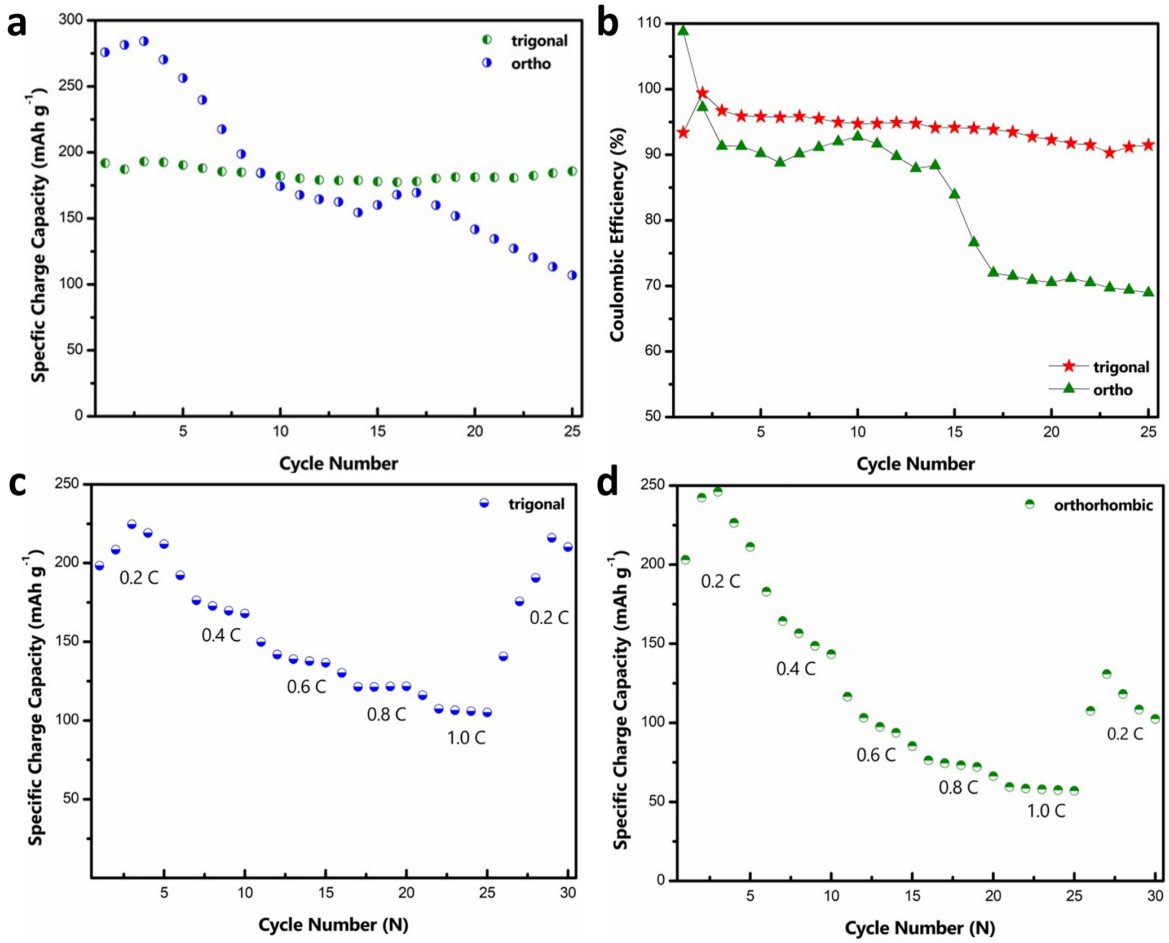

Figure 3. Cyclic stability and rate capability of MVO cathode: (**a**) Gravimetric specific capacity comparison of tri- and ortho phase at 0.4C rate; (**b**) coulombic efficiency comparison of tri- and ortho phase at 0.4C rate; (**c**,**d**) rate capability performance of the tri- and ortho phases (1C = 170 mA g ^{1}).

To understand $AlCl_4^-$ intercalation in the host MVO and the changes in the valence of Mo and V during charging and discharging, ex-situ XPS analysis of the cycled electrodes was conducted after three charge-discharge cycles. Figure 4a–c shows high-resolution Mo 3d spectra of the pristine, charged and discharged t-MVO electrodes. As mentioned earlier, in the pristine electrode, Mo is found to be in +6 (~232.90 eV) and +5 (~232.50 eV) oxidation states. Upon charging, Mo undergoes reduction to a lower oxidation state and a new peak appears at ~230 eV (+4 oxidation state). A lowering in the intensity of the higher oxidation peaks is also observed. Upon discharging, the higher oxidation state is mostly regained, however, some Mo is still found to be in the lower oxidation state. We attribute this to $AlCl_4^-$ trapped in the smaller trigonal voids (see insets in Figure 1b,c). Figure 4d–f shows high resolution spectra of V 2p for t-MVO. In the pristine electrode, the V is found predominantly to be in the +5 (~517.30 eV) oxidation state with some V also present in the +4 (516.30 eV) state. Upon charging, an increase in the intensity of the lower oxidation state is observed with a corresponding decrease in the higher oxidation state. Upon discharging, V is predominantly found to be in the higher oxidation state; however, similar to Mo, the intensity of the lower oxidation state is higher than the pristine electrode, which can again be attributed to $AlCl_4^-$ being trapped in the smaller voids. Figure 4g shows the high-resolution Al 2p spectra. As expected, the pristine electrode shows no signal for Al, while upon charging a significant increase in the Al intensity was observed. The residual Al observed in the discharged state further corroborates the fact that some $AlCl_4^-$ is trapped in the trigonal voids. Ex-situ XPS analysis of the cycled o-MVO electrode (after three cycles) was also conducted, and results are shown in Figure S7. Similar to the tri-phase, upon charging, both Mo and V undergo reduction from higher to lower oxidation states, and upon discharging the higher oxidation states are mostly recovered, with some fraction of Mo and V present in a lower oxidation state due to $AlCl_4^-$ being trapped in smaller trigonal voids.

To verify $AlCl_4^-$ insertion into MVO during cycling and to understand the elemental distribution of Mo, V, Al, and Cl inside the MVO rods, EDS mapping of the cycled electrode was conducted. Figure 5 and Figure S8 show the SEM micrograph and corresponding EDS maps of the charged t-MVO and o-MVO electrodes after five charge-discharge cycles. In addition to the uniform distribution of Mo and V, Al and Cl are also observed to be uniformly distributed in the cycled electrodes compared to pristine electrodes (Figure 1d,e) where no Al or Cl signals are observed. The SEM image of the cycled electrodes also attests to the fact the electrode structure remains intact during the battery operation.

Based on the above results, the one major attribute differentiating the performance of t-MVO and o-MVO is the coulombic efficiency (CE), which directly affects the capacity fade. Ex-situ XPS analysis shows a similar change in the chemical state for t-MVO and o-MVO during charging and discharging, and SEM analysis does not display any major changes to the morphology of the particles after cycling. Hence, to understand the cause of this difference in CE behavior, we carried out a thermogravimetric analysis of the t-MVO and o-MVO powder samples. The result (shown in Figure 6) indicates that the ortho phase has a higher tendency to retain moisture than the trigonal phase. We hypothesize that the difference in the synthesis conditions (pH and reaction time) was the cause of this difference. The reaction of residual moisture with the IL electrolyte is expected to negatively impact the CE and cycling stability performance of o-MVO relative to its t-MVO counterpart.

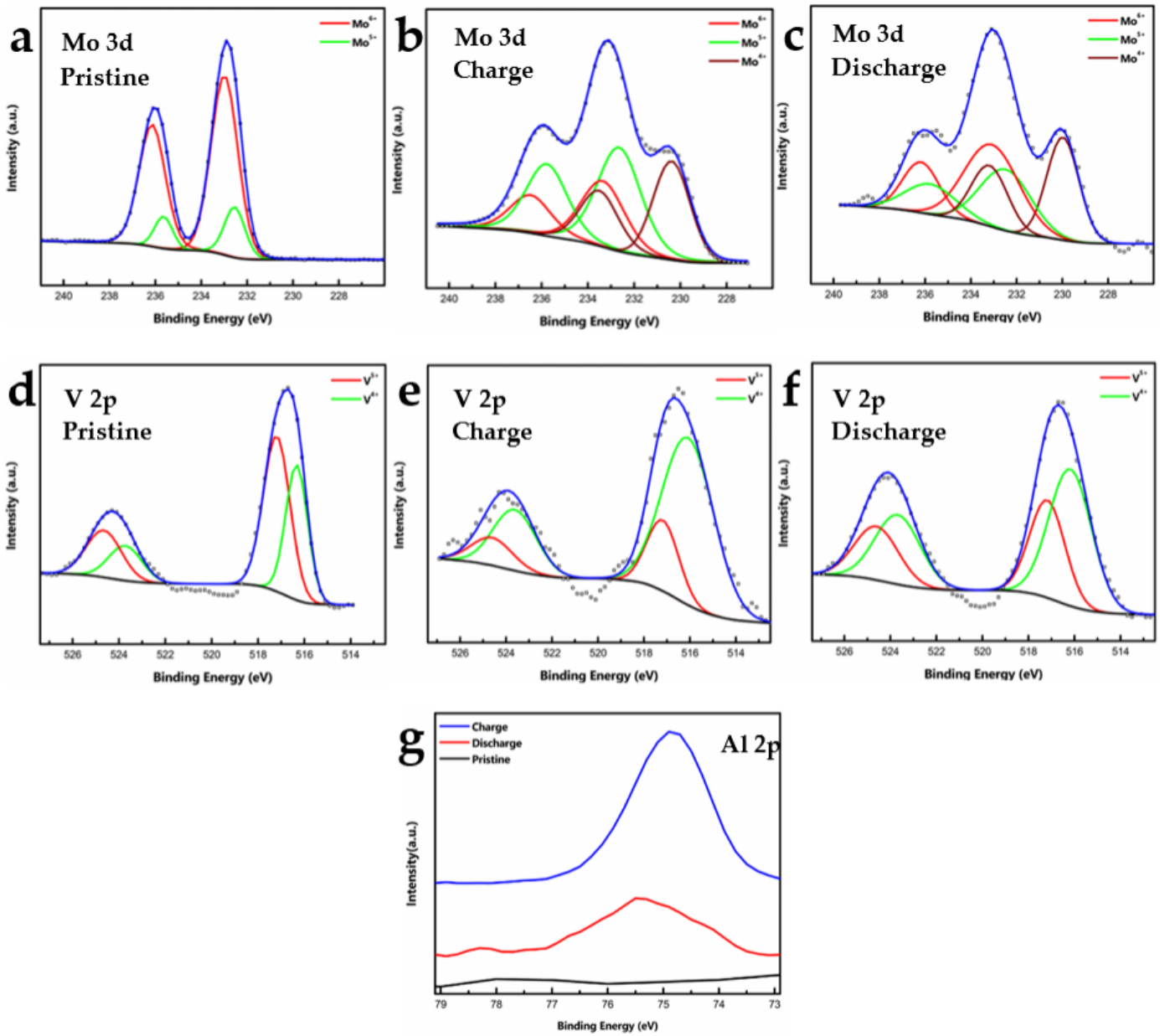

Figure 4. Ex-situ X-ray photoelectron spectroscopy analysis of cycled (3 cycles) t-MVO electrodes: (**a**–**c**) High-resolution Mo 3d spectra of electrode in pristine, charged (2.4 V), and discharged (0.02 V) states; (**d**–**f**) High-resolution V 2p spectra of electrode in pristine, charged, and discharged states; (**g**) High-resolution Al 2p spectra in pristine, charged, and discharged states. The appearance of Al 2p during charge and presence of small amount of Al 2p during discharge signifies that some amount of Al 2p is possibly trapped in the small trigonal voids of the t-MVO electrode.

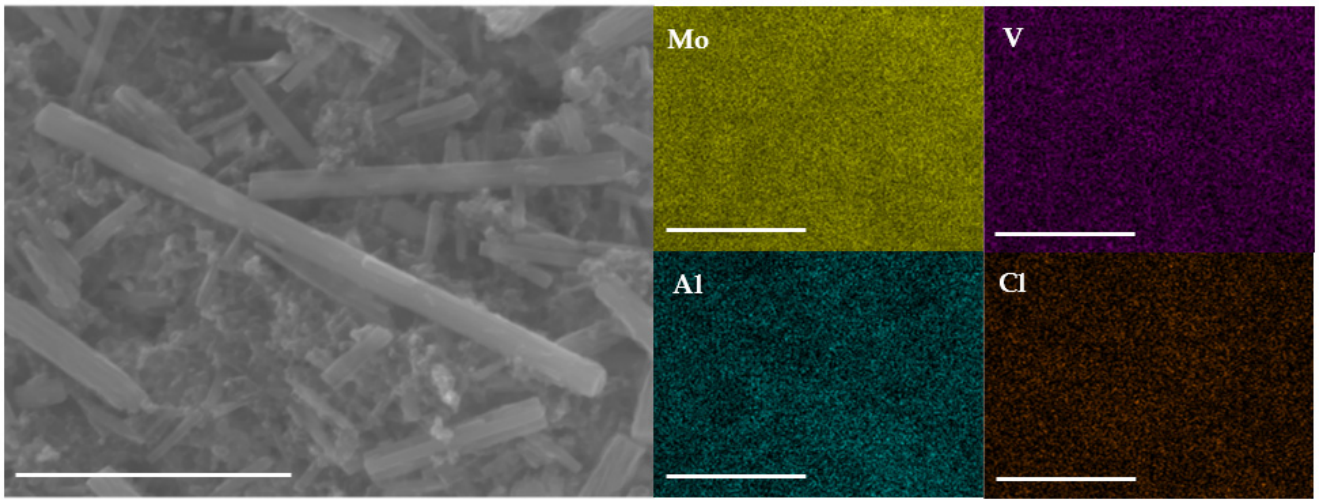

Figure 5. Ex-situ SEM and corresponding EDS mapping of the cycled (5 cycles) t-MVO electrode in the charged state. Uniform distribution of Al and Cl is clearly visible in the mapping. This signifies participation of Al and Cl during electrode cycling (scale bar: 2.5 m).

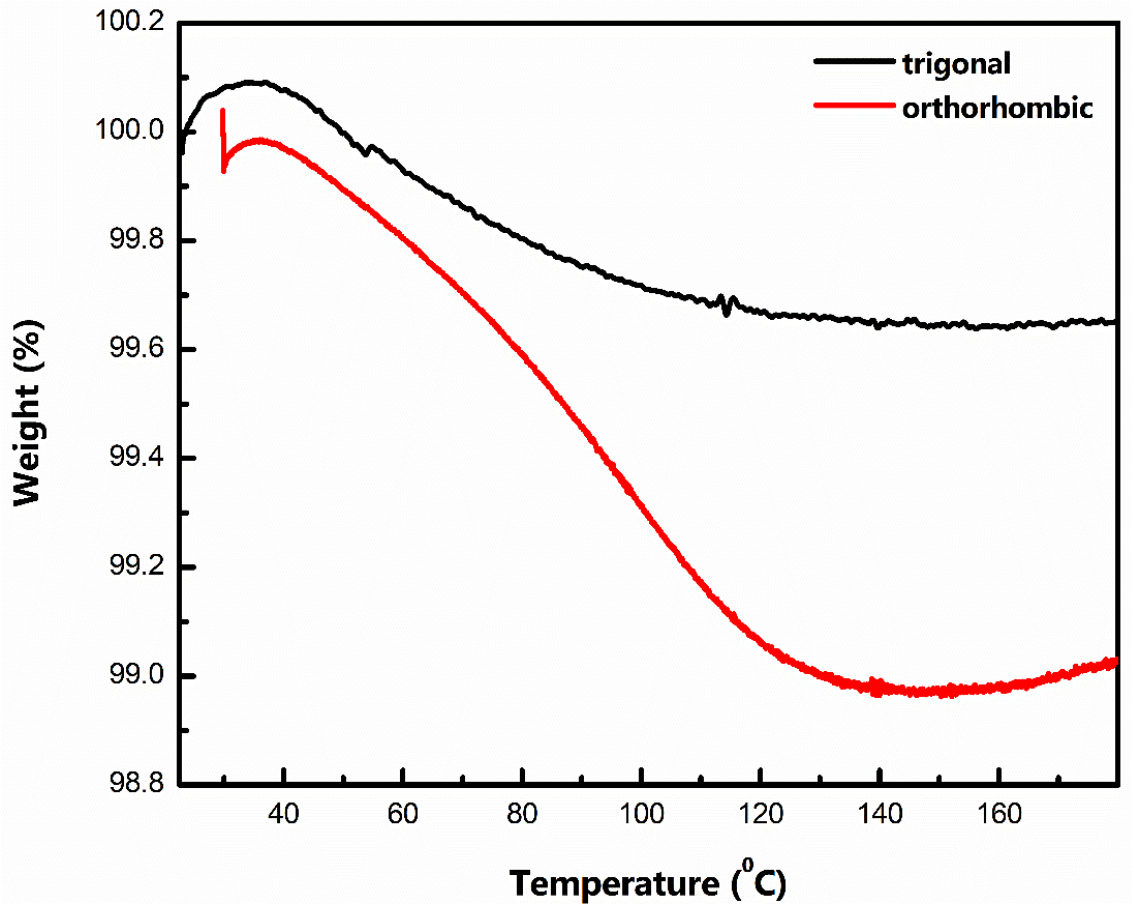

Figure 6. Thermogravimetric analysis of the tri- and ortho powder sample at a rate of 2 C/min. The water retention capacity of the ortho phase is significantly higher than that of the tri-phase.

4. Conclusion

In this study, we have reported the use of t-MVO as a high-capacity, high-rate capability host material for chloroaluminate anion intercalation. The open-tunnel framework materials were synthesized by traditional hydrothermal processing using polyoxometalate-

based chemistry. The ortho phase (o-MVO) displayed similar results as reported earlier, with a rapid capacity fade at room temperature; however, the tri-phase demonstrated better reversibility, higher coulombic efficiency, and improved rate capability than its ortho counterpart. At a charge-discharge rate of ~0.4C, t-MVO delivered a specific capacity of ~190 mAh g ^{1} with a fade rate per cycle of ~0.125%. Electrochemical measurements, followed by ex-situ analysis, confirmed the reversible insertion/de-insertion of $AlCl_4$, which may be attributed to big hexagonal and heptagonal pores (tunnels) that are ubiquitous in the MVO compounds and the minimal presence of residual moisture in the t-MVO electrode. These results indicate the promise of t-MVO as a high-performing cathode material for rechargeable Al-ion batteries. Future work should focus on in-situ XRD and TEM characterization to further confirm reversible $AlCl_4$ intercalation into the hexagonal and heptagonal pores in t-MVO, as well as irreversible entrapment of $AlCl_4$ in the smaller trigonal voids.

Supplementary Materials: The following supporting information can be downloaded at: https://www.mdpi.com/article/10.3390/batteries9020092/s1, Figure S1: XPS Analysis of the pristine electrodes. (a,b) Survey spectra of trigonal and orthorhombic electrode. Figure S2: Raman spectra of annealed orthorhombic and trigonal Mo3VOx powder samples. Figure S3: Cyclic voltammogram of trigonal phase at a high scan rate of 0.5 mV s 1. The overlapping of curves after 2nd cycle demonstrates the reversible nature of tri-electrode at higher rate. Figure S4: Discharge capacity comparison. The black curve shows near negligible capacity (~25 mAh g 1) when the first cycle is discharge cycle whereas the red curve shows almost an order of magnitude higher discharge capacity (~180 mAh g 1) when the first cycle is charge cycle. This signifies that during the charge cycle the $AlCl_4$ from the electrolyte intercalates into the MVO electrode and during the discharge cycle the $AlCl_4$ de-intercalates from the MVO electrode. Figure S5: Capacity retention performance of the ortho phase at current density of 20 mA g 1. (data obtained from ref [22]). Figure S6: Coulombic efficiency comparison of the t-MVO and o-MVO at a charge-discharge rate of 1C (1C = 170 mA g 1). The trigonal phase demonstrates a stable CE of > 97% throughout the cycles while for the ortho phase the CE shows an unstable behavior with CE fluctuating in the range of 90-95%. Figure S7: Ex-situ XPS analysis of the cycled o-MVO electrode in charged state (after 5 cycles). (a c) High resolution Mo 3d spectra of electrode in pristine, charged (2.4 V), and discharged (0.02 V) state. (d-f) High resolution V 2p spectra of electrode in pristine, charged, and discharged state. Figure S8: Ex-situ SEM and corresponding EDS mapping of the cycled o-MVO electrode in charged state. Al and Cl are observed to be uniformly distributed throughout the rod signifying participation of both Al and Cl during electrode cycling (scale bar: 2.5 m). Table S1. Comparison of electrochemical behavior of different candidate materials for non-aqueous rechargeable aluminum-ion batteries.

Author Contributions: Conceptualization, K.B. and N.K.; methodology, K.B., A.S.L., M.S. and N.K.; software, K.B., S.S., M.S. and N.K.; validation, K.B. and N.K.; formal analysis, K.B., A.S.L., S.S., M.S., V.M., R.A.P. and N.K.; investigation, K.B. and N.K.; writing—original draft preparation, K.B. and N.K.; writing—review and editing, K.B. and N.K.; visualization, K.B., S.S. and N.K.; supervision, N.K.; funding acquisition, N.K. All authors have read and agreed to the published version of the manuscript.

Funding: N.K acknowledges funding support from the USA National Science Foundation (Award Number 2126178). N.K. also acknowledges funding support from John A. Clark and Edward T. Crossan endowed Chair Professorship at Rensselaer Polytechnic Institute.

Data Availability Statement: All relevant data are provided as Datasets S1–S30, in a public repository at https://github.com/bhimak1/datasets-batteries-012023.

Acknowledgments: The authors thank David Frey and Rob Planty for their assistance with the SEM and XPS, respectively. The authors would also like to thank Fudong Han for the fruitful discussions.

Conflicts of Interest: The authors declare no conflict of interest.

References

1. Goodenough, J.B.; Park, K.-S. The Li-Ion Rechargeable Battery: A Perspective. J. Am. Chem. Soc. **2013**, 135, 1167–1176. [CrossRef]
2. Ye, L.; Li, X. A dynamic stability design strategy for lithium metal solid state batteries. Nature **2021**, 593, 218–222. [CrossRef] [PubMed]
3. Mukherjee, R.; Thomas, A.V.; Datta, D.; Singh, E.; Li, J.; Eksik, O.; Shenoy, V.B.; Koratkar, N. Defect-induced plating of lithium metal within porous graphene networks. Nat. Commun. **2014**, 5, 3710. [CrossRef] [PubMed]
4. Yu, Y.; Huang, W.; Song, X.; Wang, W.; Hou, Z.; Zhao, X.; Deng, K.; Ju, H.; Sun, Y.; Zhao, Y.; et al. Thermally reduced graphene paper with fast Li ion diffusion for stable Li metal anode. Electrochim. Acta **2019**, 294, 413–422. [CrossRef]
5. Lee, K.T.; Jeong, S.; Cho, J. Roles of Surface Chemistry on Safety and Electrochemistry in Lithium Ion Batteries. Acc. Chem. Res. **2013**, 46, 1161–1170. [CrossRef] [PubMed]
6. Leisegang, T.; Meutzner, F.; Zschornak, M.; Münchgesang, W.; Schmid, R.; Nestler, T.; Eremin, R.A.; Kabanov, A.A.; Blatov, V.A.; Meyer, D.C. The Aluminum-Ion Battery: A Sustainable and Seminal Concept? Front. Chem. **2019**, 7, 268. [CrossRef] [PubMed]
7. Komaba, S.; Murata, W.; Ishikawa, T.; Yabuuchi, N.; Ozeki, T.; Nakayama, T.; Ogata, A.; Gotoh, K.; Fujiwara, K. Electrochemical Na Insertion and Solid Electrolyte Interphase for Hard-Carbon Electrodes and Application to Na-Ion Batteries. Adv. Funct. Mater. **2011**, 21, 3859–3867. [CrossRef]
8. Yabuuchi, N.; Kubota, K.; Dahbi, M.; Komaba, S. Research Development on Sodium-Ion Batteries. Chem. Rev. **2014**, 114, 11636–11682. [CrossRef]
9. Hundekar, P.; Basu, S.; Fan, X.; Li, L.; Yoshimura, A.; Gupta, T.; Sarbada, V.; Lakhnot, A.; Jain, R.; Narayanan, S.; et al. In situ healing of dendrites in a potassium metal battery. Proc. Natl. Acad. Sci. USA **2020**, 117, 5588–5594. [CrossRef] [PubMed]
10. Yoo, H.D.; Shterenberg, I.; Gofer, Y.; Gershinsky, G.; Pour, N.; Aurbach, D. Mg rechargeable batteries: An on-going challenge. Energy Environ. Sci. **2013**, 6, 2265–2279. [CrossRef]
11. Gummow, R.J.; Vamvounis, G.; Kannan, M.B.; He, Y. Calcium-Ion Batteries: Current State-of-the-Art and Future Perspectives. Adv. Mater. **2018**, 30, 1801702. [CrossRef] [PubMed]
12. Armand, M.; Tarascon, J.-M. Building better batteries. Nature **2008**, 451, 652–657. [CrossRef] [PubMed]
13. Dunn, B.; Kamath, H.; Tarascon, J.M. Electrical energy storage for the grid: A battery of choices. Science **2011**, 334, 928–935. [CrossRef] [PubMed]
14. Amine, K.; Kanno, R.; Tzeng, Y. Rechargeable lithium batteries and beyond: Progress, challenges, and future directions. MRS Bull. **2014**, 39, 395–401. [CrossRef]
15. Van Noorden, R. The rechargeable revolution: A better battery. Nature **2014**, 507, 26–28. [CrossRef]
16. Ponrouch, A.; Frontera, C.; Bardé, F.; Palacín, M.R. Towards a calcium-based rechargeable battery. Nat. Mater. **2016**, 15, 169–172. [CrossRef]
17. Davidson, R.; Verma, A.; Santos, D.; Hao, F.; Fincher, C.; Xiang, S.; Van Buskirk, J.; Xie, K.; Pharr, M.; Mukherjee, P.P.; et al. Formation of Magnesium Dendrites during Electrodeposition. ACS Energy Lett. **2019**, 4, 375–376. [CrossRef]
18. Muldoon, J.; Bucur, C.B.; Oliver, A.G.; Sugimoto, T.; Matsui, M.; Kim, H.S.; Allred, G.D.; Zajicek, J.; Kotani, Y. Electrolyte roadblocks to a magnesium rechargeable battery. Energy Environ. Sci. **2012**, 5, 5941–5950. [CrossRef]
19. Elia, G.A.; Kravchyk, K.V.; Kovalenko, M.V.; Chacón, J.; Holland, A.; Wills, R.G.A. An overview and prospective on Al and Al-ion battery technologies. J. Power Sources **2021**, 481, 228870. [CrossRef]
20. Paranthaman, M.P.; Brown, G.; Sun, X.-G.; Nanda, J.; Manthiram, A.; Manivannan, A. A Transformational, High Energy Density, Secondary Aluminum Ion Battery. ECS Meet. Abstr. **2010**, MA2010-02, 314. [CrossRef]
21. Lin, M.-C.; Gong, M.; Lu, B.; Wu, Y.; Wang, D.-Y.; Guan, M.; Angell, M.; Chen, C.; Yang, J.; Hwang, B.-J.; et al. An ultrafast rechargeable aluminium-ion battery. Nature **2015**, 520, 324–328. [CrossRef] [PubMed]
22. Kaveevivitchai, W.; Huq, A.; Wang, S.; Park, M.J.; Manthiram, A. Rechargeable Aluminum-Ion Batteries Based on an Open-Tunnel Framework. Small **2017**, 13, 1701296. [CrossRef] [PubMed]
23. Li, J.; Tu, J.; Jiao, H.; Wang, C.; Jiao, S. Ternary $AlCl_3$-Urea-[EMIm]Cl Ionic Liquid Electrolyte for Rechargeable Aluminum-Ion Batteries. J. Electrochem. Soc. **2017**, 164, A3093. [CrossRef]
24. Wang, H.; Gu, S.; Bai, Y.; Chen, S.; Zhu, N.; Wu, C.; Wu, F. Anion-effects on electrochemical properties of ionic liquid electrolytes for rechargeable aluminum batteries. J. Mater. Chem. A **2015**, 3, 22677–22686. [CrossRef]
25. Xing, L.; Owusu, K.A.; Liu, X.; Meng, J.; Wang, K.; An, Q.; Mai, L. Insights into the storage mechanism of VS4 nanowire clusters in aluminum-ion battery. Nano Energy **2021**, 79, 105384. [CrossRef]
26. Chen, H.; Xu, H.; Wang, S.; Huang, T.; Xi, J.; Cai, S.; Guo, F.; Xu, Z.; Gao, W.; Gao, C. Ultrafast all-climate aluminum-graphene battery with quarter-million cycle life. Sci. Adv. **2022**, 3, eaao7233. [CrossRef] [PubMed]
27. Jayaprakash, N.; Das, S.K.; Archer, L.A. The rechargeable aluminum-ion battery. Chem. Commun. **2011**, 47, 12610–12612. [CrossRef]
28. Reed, L.D.; Menke, E. The Roles of V_2O_5 and Stainless Steel in Rechargeable Al–Ion Batteries. J. Electrochem. Soc. **2013**, 160, A915. [CrossRef]
29. Wang, H.; Bai, Y.; Chen, S.; Luo, X.; Wu, C.; Wu, F.; Lu, J.; Amine, K. Binder-Free V_2O_5 Cathode for Greener Rechargeable Aluminum Battery. ACS Appl. Mater. Interfaces **2015**, 7, 80–84. [CrossRef]
30. Chiku, M.; Takeda, H.; Matsumura, S.; Higuchi, E.; Inoue, H. Amorphous Vanadium Oxide/Carbon Composite Positive Electrode for Rechargeable Aluminum Battery. ACS Appl. Mater. Interfaces **2015**, 7, 24385–24389. [CrossRef]

31. Liu, S.; Pan, G.L.; Li, G.R.; Gao, X.P. Copper hexacyanoferrate nanoparticles as cathode material for aqueous Al-ion batteries. J. Mater. Chem. A **2015**, 3, 959–962. [CrossRef]
32. Geng, L.; Lv, G.; Xing, X.; Guo, J. Reversible Electrochemical Intercalation of Aluminum in Mo_6S_8. Chem. Mater. **2015**, 27, 4926–4929. [CrossRef]
33. Tong, Y.; Gao, A.; Zhang, Q.; Gao, T.; Yue, J.; Meng, F.; Gong, Y.; Xi, S.; Lin, Z.; Mao, M.; et al. Cation-synergy stabilizing anion redox of Chevrel phase Mo_6S_8 in aluminum ion battery. Energy Storage Mater. **2021**, 37, 87–93. [CrossRef]
34. Kaveevivitchai, W.; Manthiram, A. High-capacity zinc-ion storage in an open-tunnel oxide for aqueous and nonaqueous Zn-ion batteries. J. Mater. Chem. A **2016**, 4, 18737–18741. [CrossRef]
35. Lakhnot, A.S.; Bhimani, K.; Mahajani, V.; Panchal, R.A.; Sharma, S.; Koratkar, N. Reversible and rapid calcium intercalation into molybdenum vanadium oxides. Proc. Natl. Acad. Sci. USA **2022**, 119, e2205762119. [CrossRef]
36. Kaveevivitchai, W.; Jacobson, A.J. High Capacity Rechargeable Magnesium-Ion Batteries Based on a Microporous Molybdenum–Vanadium Oxide Cathode. Chem. Mater. **2016**, 28, 4593–4601. [CrossRef]
37. Sadakane, M.; Endo, K.; Kodato, K.; Ishikawa, S.; Murayama, T.; Ueda, W. Assembly of a Pentagonal Polyoxomolybdate Building Block, $[Mo_6O_{21}]^{6}$, into Crystalline MoV Oxides. Eur. J. Inorg. Chem. **2013**, 2013, 1731–1736. [CrossRef]
38. Ishikawa, S.; Ueda, W. Microporous crystalline Mo–V mixed oxides for selective oxidations. Catal. Sci. Technol. **2016**, 6, 617–629. [CrossRef]
39. Zhang, Z.; Wang, H.; Yoshikawa, H.; Matsumura, D.; Hatao, S.; Ishikawa, S.; Ueda, W. Zeolitic Vanadomolybdates as High-Performance Cathode-Active Materials for Sodium-Ion Batteries. ACS Appl. Mater. Interfaces **2020**, 12, 6056–6063. [CrossRef]
40. Inukai, S.; Ishikawa, S.; Tanabe, T.; Jing, Y.; Toyao, T.; Shimizu, K.-I.; Ueda, W. Thermally Induced Transformation of Sb-Containing Trigonal $Mo3VO_x$ to Orthorhombic $Mo3VO_x$ and Its Effect on the Catalytic Ammoxidation of Propane. Chem. Mater. **2020**, 32, 1506–1516. [CrossRef]
41. Konya, T.; Katou, T.; Murayama, T.; Ishikawa, S.; Sadakane, M.; Buttrey, D.; Ueda, W. An orthorhombic $Mo3VO_x$ catalyst most active for oxidative dehydrogenation of ethane among related complex metal oxides. Catal. Sci. Technol. **2013**, 3, 380–387. [CrossRef]
42. Wachs, I.E.; Jehng, J.-M.; Ueda, W. Determination of the Chemical Nature of Active Surface Sites Present on Bulk Mixed Metal Oxide Catalysts. J. Phys. Chem. B **2005**, 109, 2275–2284. [CrossRef] [PubMed]
43. Mitran, G.; Neaţu, F.; Pavel, O.D.; Trandafir, M.M.; Florea, M. Behavior of Molybdenum–Vanadium Mixed Oxides in Selective Oxidation and Disproportionation of Toluene. Materials **2019**, 12, 748. [CrossRef]
44. Koketsu, T.; Ma, J.; Morgan, B.J.; Body, M.; Legein, C.; Dachraoui, W.; Giannini, M.; Demortière, A.; Salanne, M.; Dardoize, F.; et al. Reversible magnesium and aluminium ions insertion in cation-deficient anatase TiO_2. Nat. Mater. **2017**, 16, 1142–1148. [CrossRef] [PubMed]
45. Geng, L.; Scheifers, J.P.; Fu, C.; Zhang, J.; Fokwa, B.P.T.; Guo, J. Titanium Sulfides as Intercalation-Type Cathode Materials for Rechargeable Aluminum Batteries. ACS Appl. Mater. Interfaces **2017**, 9, 21251–21257. [CrossRef] [PubMed]
46. Zhang, X.; Zhang, G.; Wang, S.; Li, S.; Jiao, S. Porous CuO microsphere architectures as high-performance cathode materials for aluminum-ion batteries. J. Mater. Chem. A **2018**, 6, 3084–3090. [CrossRef]
47. Li, H.; Yang, H.; Sun, Z.; Shi, Y.; Cheng, H.-M.; Li, F. A highly reversible Co3S4 microsphere cathode material for aluminum-ion batteries. Nano Energy **2019**, 56, 100–108. [CrossRef]
48. Yang, W.; Lu, H.; Cao, Y.; Xu, B.; Deng, Y.; Cai, W. Flexible Free-Standing MoS2/Carbon Nanofibers Composite Cathode for Rechargeable Aluminum-Ion Batteries. ACS Sustain. Chem. Eng. **2019**, 7, 4861–4867. [CrossRef]
49. Wang, W.; Jiang, B.; Xiong, W.; Sun, H.; Lin, Z.; Hu, L.; Tu, J.; Hou, J.; Zhu, H.; Jiao, S. A new cathode material for super-valent battery based on aluminium ion intercalation and deintercalation. Sci. Rep. **2013**, 3, 3383. [CrossRef]
50. Angell, M.; Pan, C.-J.; Rong, Y.; Yuan, C.; Lin, M.-C.; Hwang, B.-J.; Dai, H. High Coulombic efficiency aluminum-ion battery using an $AlCl_3$-urea ionic liquid analog electrolyte. Proc. Natl. Acad. Sci. USA **2017**, 114, 834–839. [CrossRef]
51. Yu, Z.; Kang, Z.; Hu, Z.; Lu, J.; Zhou, Z.; Jiao, S. Hexagonal NiS nanobelts as advanced cathode materials for rechargeable Al-ion batteries. Chem. Commun. **2016**, 52, 10427–10430. [CrossRef]
52. Wang, S.; Jiao, S.; Wang, J.; Chen, H.-S.; Tian, D.; Lei, H.; Fang, D.-N. High-Performance Aluminum-Ion Battery with CuS@C Microsphere Composite Cathode. ACS Nano **2017**, 11, 469–477. [CrossRef] [PubMed]
53. Reed, L.D.; Ortiz, S.N.; Xiong, M.; Menke, E.J. A rechargeable aluminum-ion battery utilizing a copper hexacyanoferrate cathode in an organic electrolyte. Chem. Commun. **2015**, 51, 14397–14400. [CrossRef]
54. Jiang, J.; Li, H.; Fu, T.; Hwang, B.-J.; Li, X.; Zhao, J. One-Dimensional Cu2–xSe Nanorods as the Cathode Material for High-Performance Aluminum-Ion Battery. ACS Appl. Mater. Interfaces **2018**, 10, 17942–17949. [CrossRef] [PubMed]
55. Tu, J.; Lei, H.; Yu, Z.; Jiao, S. Ordered WO_3 x nanorods: Facile synthesis and their electrochemical properties for aluminum-ion batteries. Chem. Commun. **2018**, 54, 1343–1346. [CrossRef] [PubMed]
56. Wang, S.; Yu, Z.; Tu, J.; Wang, J.; Tian, D.; Liu, Y.; Jiao, S. A Novel Aluminum-Ion Battery: Al/$AlCl_3$-[EMIm]Cl/Ni_3S_2@Graphene. Adv. Energy Mater. **2016**, 6, 1600137. [CrossRef]